THE ASTROPHYSICAL JOURNAL, 387:69–82, 1992 March 1
© 1992. The American Astronomical Society. All rights reserved. Printed in U.S.A.

INSTABILITIES IN ASTROPHYSICAL JETS. I. LINEAR ANALYSIS OF BODY AND SURFACE WAVES

JUN-HUI ZHAO
National Radio Astronomy Observatory,[1] P.O. Box O, Socorro, NM 87801[2]; and Institute for Astrophysics, University of New Mexico, Albuquerque, NM 87131

JACK O. BURNS
Department of Astronomy, New Mexico State University, Las Cruces, NM 88003

PHILIP E. HARDEE
Department of Physics and Astronomy, University of Alabama, Tuscaloosa, AL 35487

AND

MICHAEL L. NORMAN
National Center for Supercomputing Applications and Department of Astronomy, The Beckman Institute, University of Illinois, Urbana, IL 61801

Received 1989 November 1; accepted 1991 August 30

ABSTRACT

In this paper, we investigate the instabilities of astrophysical jets in a new and more generalized way than in previous studies. We solve the dispersion equations for a thermally confined slab jet in a complex (k, ω) domain. We find a number of singularities related to certain wave modes in this system. We show that the internal jet flow in the system is characterized by two internal sound waves, propagating against and with the flow, respectively. These two body waves grow in amplitude. The one propagating against the flow is condensed, which is crucial to disruption of jets. The other, propagating with the flow, is rarefied and less important in jet disruption. In addition, there are a number of surface waves existing in the interface between the jet flow and the ambient medium. Two of them are identified to couple to their relevant acoustic body waves. They also grow in amplitude. Our study in this paper suggests that the growing internal body waves and abundant growing surface waves can potentially explain the wealth of observed phenomena in astrophysical jets, such as quasi-periodic wiggles, jet disruption, limb-brightened features, and surface filaments. It also is a great help in understanding the plentiful features observed in numerical simulations. The predictions made in this paper will be directly compared with two-dimensional nonlinear numerical simulations in Paper II.

Subject headings: galaxies: jets — hydrodynamics — instabilities — methods: numerical — shock waves

1. INTRODUCTION

There is growing evidence from high-resolution observations that radio emitting jets in active galaxies interact in a substantial way with their environments. Bent jets and radio tails associated with head-tail radio sources in clusters of galaxies appear to be particularly striking examples of strong interactions between outflowing radio plasma and the intergalactic medium. The radio jets emanating from the galaxy cores in wide-angle tailed (WAT) sources are initially very straight, well collimated, and probably supersonic, but they disrupt (i.e., decollimate) and bend abruptly in the outer galaxy halos (Norman, Burns, & Sulkanen 1988; Burns, Norman, & Clarke 1986). Recently, extensive radio observations with the Very Large Array (VLA) (e.g., O'Donoghue, Owen, & Eilek 1990) have shown substantial evidence that jets in WATs appear to wiggle and flare as the jets disrupt (e.g., radio sources 1321+674 in Abell 1559 and 0110+152 in Abell 160.) This morphology suggests that certain unstable wave modes grow in the jet flows. One possible mechanism for the disruption of astrophysical jets utilizes the Kelvin-Helmholtz (hereafter K-H) instability. This paper reports the results of a generalized study of instabilities in astrophysical jets as a means to better understand the nature of the structure in and disruption of collimated outflows.

The K-H instability is a well-known phenomenon in fluid mechanics and astrophysics. Since the original proposal of the fluid beam hypotheis (Scheuer 1974; Blandford & Rees 1974) for the production of jets in energetic radio galaxies, a K-H instability analysis has been performed by many authors in either a linear perturbation regime (e.g., Blandford & Pringle 1976; Ferrari et al. 1978, 1981, 1982; Hardee 1979, 1982, 1983, 1984, 1986, 1987; Hardee & Norman 1988; Ray 1981; Cohn 1983; Payne & Cohn 1985) or a nonlinear numerical simulation regime (Norman, Winkler, & Smarr 1984; Norman & Hardee 1988).

The linearized dispersion relation equations in both slab and cylindrical geometries were first derived by Gill (1965). Numerical solutions of the equations using a fixed real frequency (ω) and/or a fixed real wavenumber (k) were used to study the so-called spatial and/or temporal instability mode structures of a thermally confined jet, respectively. For a cylindrically symmetric, thermally confined jet, perturbations to the jet are described in terms of harmonic components associated with different Fourier modes which are an axisymmetric pinching mode, a nonaxisymmetric helical mode, and higher order harmonic (or fluting) modes (Hardee 1979; Ferrari et al. 1981). Each mode consists of a fundamental mode and reflection modes (Hardee 1979; Ferrari et al. 1981). For a two-dimensional symmetric jet, only two types of modes exist; they

---

[1] The National Radio Astronomy Observatory is operated by Associated Universities, Inc., by cooperative agreement with the National Science Foundation.

[2] Postal address.

© American Astronomical Society • Provided by the NASA Astrophysics Data System

1992ApJ...387...69Z

are an axisymmetric pinching mode and an antisymmetric sinusoidal mode (see Fig. 9 below) (Gill 1965; Hardee & Norman 1988). Again, each mode consists of a fundamental and reflection modes.

The predictions made by linear theory have recently been compared with numerical simulations in a nonlinear regime (Norman & Hardee 1988). In general, results from the simulations agree with the predictions of linear theory. The two-dimensional simulations of slab-symmetric jets show that a perturbation imposed by sinusoidal wiggling is unstable; the collimated jet is disrupted and a turbulent lobe is formed. Norman & Hardee (1988) have concentrated on the comparison of the growth rates predicted by the linear theory and the disruption behavior in a nonlinear regime using different driving frequencies. They found that the jet disrupted in about seven *e*-folding lengths as predicted by the linear theory (Hardee & Norman 1988).

Our new work is a generalization of the analysis of instabilities in a thermally confined jet. Based on this analysis, we are able to better understand the wave phenomena developing in jets. The eigenvalue system of a thermally confined slab jet contains many more normal modes than those described in previous studies where a fixed real frequency and/or a fixed real wavenumber was assumed. Gill (1965) pointed out that there is a resonance such that sound waves impinging on the boundaries at certain angles release large amounts of energy. Thus, the K-H instability is no longer restricted to surface waves because the energy is carried by the internal sound waves from one side of the jet to the other such that the two sides of the jet communicate by the sound waves through the internal medium. The reflection effect has been considered in recent studies (Ferrari et al. 1981, 1982; Cohn 1983; Payne & Cohn 1985; Hardee & Norman 1988), but the relation between growing modes and internal waves such as sound waves was ignored in the previous studies because of the incomplete analysis of the roots of the dispersion relation. In addition to fixed real ω (spatial) and/or fixed real k (temporal) solutions considered in previous studies, there are complex root solutions to the dispersion relation.

In the present work, we provide a method for extraction of all roots from the dipsersion equations for a slab jet. The solutions are presented on a complex, inverse velocity plane. We find that there are eight singularities in the plane. The positions of the singularities are determined by the internal Mach number ($M_{\rm in} \equiv u_0/a_{\rm in}$) and the density ratio ($\eta \equiv \rho_{\rm in}/\rho_{\rm ex}$), and are independent of the harmonic modes. These singularities are associated with different types of waves. In general, there are two types of waves determined by the jet boundary conditions. First, waves propagating through the body of a fluid (or only existing in the interior of the medium) are called *body waves*, such as acoustic waves. The effect of boundaries upon such waves (e.g., reflection and refraction) is secondary since the existence of the waves is not determined by the presence of the boundaries. For instance, body waves will propagate in an infinite medium. The role of the boundaries becomes important when the jet is thermally confined. The effect of reflection of internal body waves on such boundaries leads to the growing modes which will eventually cause disruption of the jet. The second class of waves depends strongly upon the existence of boundaries. The waves and ripples on the surface of water are familiar examples. Since the existence of these waves depends upon the presence of a discontinuous surface, they are usually called *surface waves.* Both types of waves likely play roles in determining the morphology of radio jets.

The effects of these two types of waves on jet instability and disruption remains ambiguous despite the significant past analyses. Therefore, we need to address the following questions:

1. How many body and surface waves exist in a thermally confined jet?
2. Which waves play the most important role in the instability and/or disruption of the jet?
3. Is it possible to identify the different type of waves in numerical simulations?

In this paper we will theoretically study the relation between the waves and growing modes. We will compare the predictions from the linear theory with numerical simulations to identify the different types of waves in a companion paper (Zhao et al. 1992, hereafter Paper II).

The outline of this paper is as follows. In § 2, we extract the complex solutions of the linearized dispersion equations and present analytic forms for the eight singularities. In § 3, we numerically present the complex solutions ($\tilde{k}_R$, $\tilde{k}_I$, $\tilde{\omega}_R$, and $\tilde{\omega}_I$) in the inverse velocity plane and compare with solutions derived for fixed real frequency. In § 4, considering boundary conditions, we show that two of the eight singularities are associated with acoustic body waves. The remaining six are shown to be surface waves that depend on the boundaries. In § 5, we show that these body and surface waves are unstable and suggest that the fast growing one will substantially disrupt the collimation of the jet. In § 6, we discuss and summarize the results.

2. THE COMPLETE ROOTS FROM THE DISPERSION EQUATIONS FOR A SLAB JET

2.1. *Motivation*

Linear perturbation theory seeks to predict the development in time and space of an arbitrarily small disturbance of a physical system. This leads to linearization of the fluid equations and to the resolution of the arbitrary disturbance into independent wave components of Fourier normal modes. Under certain boundary conditions, the initial value problem becomes an eigenvalue problem which leads to solving the dispersion relation of the form

$$F(\omega, k) = 0 . \tag{1}$$

This relation may be regarded as determining either the complex frequency ω for any real wavenumber k, or k for any real value of ω, or as determining the complete functional relationship between the complex variables ω and k that has been emphasized by a number of authors (e.g., Drazin & Reid 1985; Gaster 1965). Clearly, either the temporally growing modes (with fixed real wavenumber k) or spatially growing modes (with fixed real frequency ω) are only a part of the solutions of the eigensystem. For example, the spatial modes behave like $\exp[i(kz - \omega t)] = \exp[-k_I z + i(k_R z - \omega t)]$ and so they grow or decay with z, unless $k_I = 0$ (system oscillates in z with wavelength $2\pi/k_R$). These spatial modes resemble a forced oscillation with a source frequency ω; so, one might think that the criterion of instability of the flow is simply that $-k_I > 0$ for some real value of ω, but unfortunately the criterion is not always as simple as that. In fact, in this paper we study the linear development of an arbitrary perturbation rather than a forced oscillation. A general perturbation function of a small disturbance can be understood as a composition of Fourier components with complex wave number k and

© American Astronomical Society • Provided by the NASA Astrophysics Data System

1992ApJ...387...69Z

complex frequency ω (Gaster 1965). The traditional spatial-growing mode technique used in astrophysical jets has a limit in understanding the relationship between the individual growing modes and waves. Certainly, analysis of the complete relation of the complex variables ω and k is necessary in understanding the linear development of a general perturbation in an astrophysical jet.

2.2. *Structure of the Roots*

Instead of cylindrical geometry, we use a slab geometry to study the instabilities in astrophysical jets in this paper. There are two reasons for using this approach. First, the physics of jets in both geometries are very similar. As mentioned in the previous section, the difference of the mode structure between slab and cylindrical jets is that the later one contains more high-order fluting modes which are important only at high frequency and/or larger wavenumber. We are not interested in these types of modes here. Also, at the long-wavelength limit, the dispersion equations for a cylindrical jet are analogous to ones in slab geometry. Second, we plan to directly compare the predictions from the linear analysis here with two-dimensional numerical simulations which are also in slab symmetry (Paper II).

The dispersion equations of symmetric and antisymmetric modes for a thermally confined slab jet can be expressed as (Hardee & Norman 1988)

$$\tan(\tilde{\beta}_{\rm in}) = -i\eta\,\frac{\tilde{\beta}_{\rm ex}}{\tilde{\beta}_{\rm in}}(1-\phi)^2\,, \tag{2a}$$

$$\cot(\tilde{\beta}_{\rm in}) = +i\eta\,\frac{\tilde{\beta}_{\rm ex}}{\tilde{\beta}_{\rm in}}(1-\phi)^2\,; \tag{2b}$$

where $\phi = \tilde{k}/\tilde{\omega} = \tilde{v}^{-1}$, is a dimensionless, complex inverse velocity scaled by jet velocity u_0; R is the radius of the jet (half width of the slab jet); η is the ratio of internal jet density to external density; $\tilde{k}$ and $\tilde{\omega}$ are dimensionless wavenumber and frequency scaled by R and R/u_0, respectively; $\tilde{\beta}_{\rm in} = \{\tilde{\omega}^2[M_{\rm in}^2(1-\phi)^2 - \phi^2]\}^{1/2}$ and $\tilde{\beta}_{\rm ex} = [\tilde{\omega}^2(M_{\rm ex}^2 - \phi^2)]^{1/2}$ are dimensionless transaction wavenumbers, scaled by R, for the internal and external medium, respectively. The internal and external Mach numbers, $M_{\rm in}$ and $M_{\rm ex}$, are determined by the jet velocity and the internal and external sound velocity, respectively.

Equation (2a) corresponds to the axisymmetric pinching mode and equation (2b) corresponds to the antisymmetric sinusoidal mode (see Fig. 9.) We note that it is only necessary to consider the wave propagation in the same direction as jet velocity u_0, namely, $\theta = 0$ (θ is the angle between wave and jet velocity vectors) as the wave propagation at an angle $\theta \neq 0$ can be obtained by replacing the jet velocity u_0 by $u_0 \cos\theta$ (Miles & Fejer 1963; Gill 1965).

Substituting

$$\tan(\tilde{\beta}_{\rm in}) = -i\,\frac{\exp(i\tilde{\beta}_{\rm in}) - \exp(i\tilde{\beta}_{\rm in})}{\exp(i\tilde{\beta}_{\rm in}) + \exp(i\tilde{\beta}_{\rm in})}\,, \tag{3a}$$

$$\cot(\tilde{\beta}_{\rm in}) = +i\,\frac{\exp(i\tilde{\beta}_{\rm in}) + \exp(i\tilde{\beta}_{\rm in})}{\exp(i\tilde{\beta}_{\rm in}) - \exp(i\tilde{\beta}_{\rm in})}\,, \tag{3b}$$

into equation (2), one can rewrite the dispersion equation as

$$\tilde{\beta}_{\rm in} = m\pi - \frac{i}{2}\ln(D_\pm)\,, \tag{4a}$$

$$D_\pm = \frac{1 \pm \eta(1-\phi)^2\sqrt{M_{\rm ex}^2 - \phi^2}/\sqrt{M_{\rm in}^2(1-\phi)^2 - \phi^2}}{1 - \eta(1-\phi)^2\sqrt{M_{\rm ex}^2 - \phi^2}/\sqrt{M_{\rm in}^2(1-\phi)^2 - \phi^2}}\,; \tag{4b}$$

where " + " corresponds to symmetric mode and " − " corresponds to antisymmetric mode; each mode consists of a series of fundamental and reflection modes represented by an integer number m; $m = 0$ corresponds to a fundamental mode (Hardee & Norman 1988); and $m = 1, 2, \ldots$ corresponds to different orders of reflection modes.

Actually, the minus sign in D_- contributes $\pi/2$ to the real part in equation (4); therefore, we can rewrite equation (4) as

$$\tilde{\beta}_{\rm in} = {\rm zm}\,\pi - \frac{i}{2}\ln(D)\,, \tag{5a}$$

$$D = \frac{1 + \eta(1-\phi)^2\sqrt{M_{\rm ex}^2 - \phi^2}/\sqrt{M_{\rm in}^2(1-\phi)^2 - \phi^2}}{1 - \eta(1-\phi)^2\sqrt{M_{\rm ex}^2 - \phi^2}/\sqrt{M_{\rm in}^2(1-\phi)^2 - \phi^2}}\,; \tag{5b}$$

where ${\rm zm} = m + \frac{1}{2}$; then, ${\rm zm} = 0, 1, 2, \ldots$ correspond to the symmetric modes, and ${\rm zm} = 1/2, 3/2, 5/2, \ldots$ correspond to the antisymmetric modes. It follows that the dimensionless frequency $\tilde{\omega}$ can be directly expressed as a function of the complex, inverse velocity ϕ:

$$\tilde{\omega} = \frac{1}{\sqrt{M_{\rm in}^2(1-\phi)^2 - \phi^2}}\left[{\rm zm}\,\pi - \frac{i}{2}\ln(D)\right], \tag{6}$$

and the dimensionless wavenumber $\tilde{k}$ is

$$\tilde{k} = \phi\tilde{\omega}\,. \tag{7}$$

Expressed in this form, $\tilde{\omega}$ and $\tilde{k}$ become functions of ϕ with a few notable singularities, and we can find the complete root structure in the complex ϕ plane. This technique differs considerably from what has been done in the past. We are able to solve for the singularities in the system and therefore to cover a broad regime in the complex $(\tilde{k}, \tilde{\omega})$ domain.

2.3. *Singularities on the Complex ϕ-Plane*

There are eight singularities on the complex, inverse velocity plane. In § 2.4 we will show that the singularities correspond to various types of waves in the eigenvalue system. From equation (6) and/or equation (7), two of the singularities are given by

$$M_{\rm in}^2(1-\phi)^2 - \phi^2 = 0\,, \tag{8}$$

and they are

$$\phi_1^\pm = \frac{M_{\rm in}}{M_{\rm in} \pm 1}\,.$$

And the other six are given by solving $D = 0$ and/or $D = \infty$, namely,

$$M_{\rm in}^2(1-\phi)^2 - \phi^2 - \eta^2(1-\phi)^4(M_{\rm ex}^2 - \phi^2) = 0\,. \tag{9}$$

Two of the six have simple forms and are given by

$$\phi_2^\pm = 1 \pm \eta^{-1/2}\,;$$

and the other four are more complicated. We present analytic forms only in two limited cases: (1) extremely subsonic, $M_{\rm in} \to 0$ and (2) supersonic where the condition

$$M_{\rm in}^2 > \eta + 1 + 3\eta^{1/3}M_{\rm in}^{2/3} \tag{10}$$

is satisfied. Note that this corresponds to $M_{\rm in} > 1.772$ with $\eta = 0.1$. For the supersonic case, the remaining four singularities are real and can be expressed as

$$\phi_3^\pm = \left(\frac{1}{2} + \frac{\delta}{2}\right) \pm \frac{1}{2}\sqrt{(1-\delta)^2 - \frac{4}{\eta}\left[y + \frac{(1-y)}{\delta}\right]}\,;$$

$$\phi_4^\pm = \left(\frac{1}{2} - \frac{\delta}{2}\right) \pm \frac{1}{2}\sqrt{(1+\delta)^2 - \frac{4}{\eta}\left[y + \frac{(1-y)}{\delta}\right]}\,;$$

© American Astronomical Society • Provided by the NASA Astrophysics Data System

1992ApJ...387...69Z

where

$$\delta = \sqrt{(2y + M_{\rm in}^2 - 1)/\eta} \; ;$$
$$y = \frac{f}{3} \cos\left[\frac{1}{3} \cos^{-1}\left(\frac{54\eta M_{\rm in}^2}{f^3} - 1\right)\right] - \frac{f}{6} \; ;$$
$$f = M_{\rm in}^2 - \eta - 1 \; .$$

We also performed numerical calculations of the singularities over the transonic region extending from internal jet Mach number 0–5. The eight singularities are plotted in Figure 1 as a function of $M_{\rm in}$ with fixed $\eta = 0.1$, where each singularity has a real part, ϕ_R, and an imaginary part, ϕ_I. In the supersonic region, we see that ϕ_3^+ and ϕ_4^+ are very close to ϕ_1^- and ϕ_1^+, respectively. As the jet becomes transonic, $\phi_3^\pm$ form a complex conjugate pair. The point of bifurcation is given by equation (10); for $\eta = 0.1$, it is at $M_{\rm in} = 1.772$. When $M_{\rm in}$ becomes small, the four singularities can be expressed in simple forms as

$$\phi_3^\pm = 1 \pm i1/\sqrt{\eta} \; ;$$
$$\phi_4^\pm = \pm M_{\rm in}/\sqrt{1 + \eta} \; .$$

When $M_{\rm in}$ becomes large, the four singularities become

$$\phi_3^\pm = \begin{cases} 1 + 1/(M_{\rm in}^2 - 1) \; ; \\ \sqrt{(M_{\rm in}^2 - 1)/\eta} + 1/(M_{\rm in}^2 - 1) \; ; \end{cases}$$
$$\phi_4^\pm = \begin{cases} 1 - 1/(M_{\rm in}^2 - 1) \; ; \\ -\sqrt{(M_{\rm in}^2 - 1)/\eta} + 1/(M_{\rm in}^2 - 1) \; . \end{cases}$$

2.4. *Reflection and Transmission Coefficients*

To investigate the nature of the singularities on a slab jet let us introduce the complex reflection and transmission coefficients (R and T) for a wave incident on the jet boundary (e.g., Payne & Cohn 1985):

$$R \equiv \frac{Z_{\rm ex} - Z_{\rm in}}{Z_{\rm ex} + Z_{\rm in}} \; , \tag{11}$$

$$T \equiv \frac{2Z_{\rm ex}}{Z_{\rm ex} + Z_{\rm in}} \; , \tag{12}$$

$$T = 1 + R \; ,$$

where Z is the normal acoustic impedance at the boundary (defined as the ratio of the pressure to the normal velocity). The subscripts "in" and "ex" represent the internal and external medium, respectively. It can be shown that (e.g., Hardee & Norman 1988)

$$R = D^{-1} = \frac{(\tilde{\beta}_{\rm ex} - \tilde{\beta}_{\rm in})(\tilde{\beta}_{\rm in}\tilde{\beta}_{\rm ex} - \tilde{k}^2)}{(\tilde{\beta}_{\rm ex} + \tilde{\beta}_{\rm in})(\tilde{\beta}_{\rm in}\tilde{\beta}_{\rm ex} + \tilde{k}^2)} \; . \tag{13}$$

The reflection and transmission coefficients are related to a wave incident upon the interface between the internal and external media of a jet, and the singularities in the dispersion relation emerge from the waves interacting with the boundaries. Miles (1957) pointed out that there is a resonance when the denominator of equations (11) and (12) vanishes. It is interesting to investigate the relationship between the singularities and the resonances. First, the two singularities, $\phi_1^\pm$, occur at $R = -1$ and $T = 0$. Physically, this corresponds to the waves trapped inside the jet by the external medium (Payne & Cohn 1985). In § 4, we will show that they correspond to internal acoustic body waves. Second, the other six of the eight singularities occur at $R = 0$ and $T = 1$, where the incident wave transmits all the energy to the external medium. The singularities arise from the waves that propagate only along the interface of the jet. These types of waves are appropriately referred to surface waves in § 4. Among the six singularities, ϕ_4^+ and ϕ_3^+ couple to ϕ_1^+ and ϕ_1^-, respectively. Finally, the resonances occur when the denominator of equations (11) and (12) vanishes, and R and T go to infinity. Thus, the reflected and transmitted waves have amplitudes much greater than the amplitudes of the incident wave. Many efforts had been made to find this type of the resonance in a thermally confined jet (e.g., Payne & Cohn 1985; Hardee & Norman 1988) and the previous results were not explicit. In fact, the resonances occur at the same phase velocities where we find the singularities of the surface waves, provided the transaction wave numbers of external and internal media, $\tilde{\beta}_{\rm ex}$ and $\tilde{\beta}_{\rm in}$, have different signs. We note that this type of resonance may occur under a particular initial perturbation condition such that the internal and external waves interact at the jet interface. In the rest of this paper, we are mainly concerned with the instabilities that emerge from the body and surface waves.

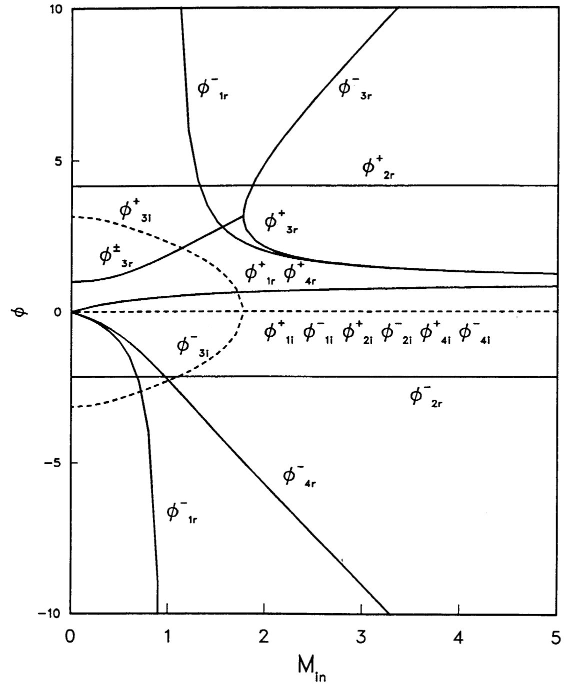

FIG. 1.—The singularities of thermally confined jet with slab geometry are plotted as function of internal Mach number with density ratio $\eta = 0.1$.

3. NUMERICAL SOLUTIONS OF THE DISPERSION EQUATIONS

3.1. *Eigenroot Structures on the ϕ-Plane*

In § 2, we located the eight singularities in supersonic and subsonic regions. The transonic region is very complicated. In what follows, we present the eigenroots only in the supersonic region. In this region, all singularities are real. As an example, we concentrate on the case with $M_{\rm in} = 3$ and $\eta = 0.1$. In Figure 2, we plot the eight singularities on the ϕ-plane. The most interesting region on the ϕ-plane is the region around the five singularities enclosed by the square indicated in Figure 2. The instabilities that emerge from the acoustic waves are located in

1992ApJ...387...69Z

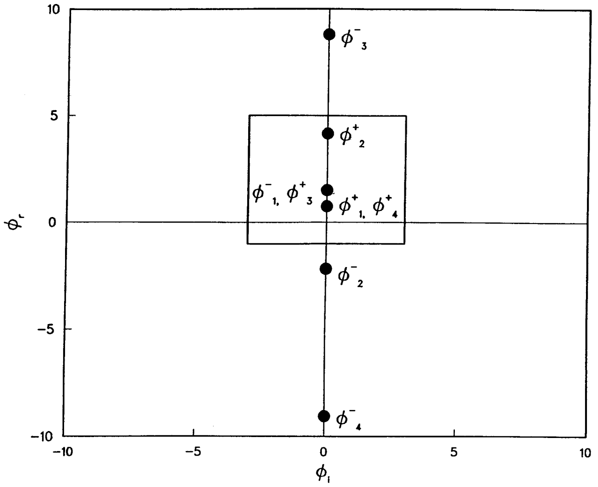

FIG. 2.—The positions (*filled circles*) of the eight singularities on the complex inverse velocity (ϕ) plane are plotted with $M_{\rm in} = 3$ and $\eta = 0.1$. Circles ϕ_1^- and ϕ_1^+ are overlapped with circles ϕ_3^+ and ϕ_4^+, respectively.

this region. Also, there is one surface wave, ϕ_2^+ included in the region. The instabilities that emerge from the other three surface waves are similar to those from ϕ_2^+. We will mainly focus on the instabilities related to the enclosed five singularities.

The negative imaginary part of the k, namely $-k_I$, is the spatial growth rate and, similarly, ω_I is the temporal growth rate where the normal mode has the form $f = A \exp\{i(k_R z - \omega_R t)\} \exp(-k_I z + \omega_I t)$. We have solved for the dimensionless frequency and wavenumber in equations (6) and (7) for zm = 0, 1/2, 1, 3/2. The solutions of $\tilde{\omega}_R$, $\tilde{\omega}_I$, $\tilde{k}_R$, and $-\tilde{k}_I$ in the square region are presented as three-dimensional views on the complex ϕ-plane (Figs. 3, 4, 5, and 6 corresponding to zm = 0, 1/2, 1, and 3/2, respectively). Generally, structure of the fundamental symmetric mode (zm = 0) is different from the fundamental antisymmetric (zm = $\frac{1}{2}$) and all of the reflection modes (zm $\geq$ 0). The fundamental antisymmetric mode has structure similar to the reflection modes. The fastest temporally or spatially growing modes are associated with the five singularities. For zm = 0, the root structure associated with spatial and temporal growth rates ($\tilde{k}_I$ and $\tilde{\omega}_I$) is symmetric about the real axis of ϕ (Figs. 3*a* and 3*b*). Perturbed waves decay temporally but grow spatially in the region around the five singularities except for the region between the singularities ϕ_1^+ and ϕ_1^- where the wave modes grow temporally but decay spatially. For the antisymmetric fundamental mode (zm = $\frac{1}{2}$) and the higher order reflection modes (zm $\geq$ 1), the root structure of spatial and temporal growth is similar but the spatial and/or temporal growth rate increases as the value of zm increases. Note that all nonzero zm modes behave differently from the zm = 0 mode. The symmetry about the real axis on the complex ϕ-plane is broken for the nonzero zm modes (Figs. 4, 5, and 6). Similar to the zm = 0 mode, most spatially growing roots correspond to temporal decay and temporally growing roots correspond to spatial decay.

3.2. *Roots with Fixed Real* ω

Most previous work on jet instabilities has focused on the roots with a fixed real frequency or fixed real wavenumber (e.g., the work in a slab geometry done by Hardee & Norman 1988). Obviously, roots with a fixed real frequency or wavenumber are only a limited case of our more general solutions. Let us compare our present results with those of Hardee & Norman (1988). The frequency $\tilde{\omega}$ and wavenumber $\tilde{k}$ can be expressed as

$$\tilde{\omega} = \tilde{\omega}_R + i\tilde{\omega}_I \; ; \tag{14a}$$

$$\tilde{k} = \tilde{k}_R + i\tilde{k}_I \; . \tag{14b}$$

Spatial growth investigated by Hardee & Norman (1988) corresponds to the roots with $\tilde{\omega}_I(\phi_R, \phi_I) = 0$. We have used the complex root finder ZANLYT in IMSL to calculate the roots with fixed real $\tilde{\omega}$. We plot the spatial growth rate $(-\tilde{k}_I)$ versus $\tilde{\omega}$ for the two fundamental modes (zm = 0 and $\frac{1}{2}$) and the first two reflection modes (zm = 1 and 3/2) in Figure 7. To compare with solutions derived in the previous section, we also show the relevant tracks of the roots on the complex ϕ-plane in Figure 8. We have compared these restricted solutions with the ones derived in the generalized way described in § 3.1, and they are consistent with each other.

Several additional comments are worth making here for Figure 8. We note that for each zm mode, the frequency increases toward the singularities ϕ_1^- and ϕ_3^+ along the curves labeled by zm = 0, 1/2, 1, and 3/2 in Figure 8. Along the curve labeled zm = 0 towards the singularities ϕ_1^- and ϕ_3^+, the phase velocity of zm = 0 modes decreases from u_0 to $\frac{2}{3}u_0$ which corresponds to the acoustic waves propagating against the jet flow in an observer's frame; and the phase velocity of nonzero zm mode increases from zero to $\frac{2}{3}u_0$. It indicates that all the growing modes derived by assuming the fixed real frequency in the previous studies (e.g., Hardee & Norman 1988) are associated with one singularity composed of an acoustic body wave and the relevant surface wave, propagating against the flow. This indicates that the acoustic wave, propagating against the flow is the most important one in the system. These growing modes associated with this wave have been intensively studied in previous work. However, the other waves were unfortunately ignored.

4. WAVES IN A THERMALLY CONFINED SLAB JET

In § 2, we found eight singularities associated with the slab jet with thermally confined boundaries. The singularities originating from incident waves in a supersonic jet have been briefly discussed in the previous sections. In the following, we will discuss the nature of the waves associated with the singularities.

These singularities represent (case a) body waves, such as sound waves, which propagate in the interior of uniform media. The existence of such waves is independent of boundaries, although the boundaries introduce reflection and refraction of the waves (Gill 1965; Payne & Cohn 1985). In addition to body waves, the singularities represent (case b) surface waves. In contrast to body waves, the boundary and/or the surface of discontinuity is necessary to the propagation of these waves. Energy trapping by the boundaries leads to the surface waves. The existence of discontinuous boundaries is a *necessary* condition to the propagation of such waves. Figure 9 illustrates the symmetric (case *a*) and antisymmetric (case *b*) surface wave patterns which occur in a thermally confined slab jet. In addition, there are short-wavelength, high-frequency surface ripples.

Body waves and surface waves in the slab jet can be distinguished by examining the role of the boundaries. In practice, this can be accomplished by investigating two typical jet boundaries. First, we consider a perfectly rigid boundary

© American Astronomical Society • Provided by the NASA Astrophysics Data System

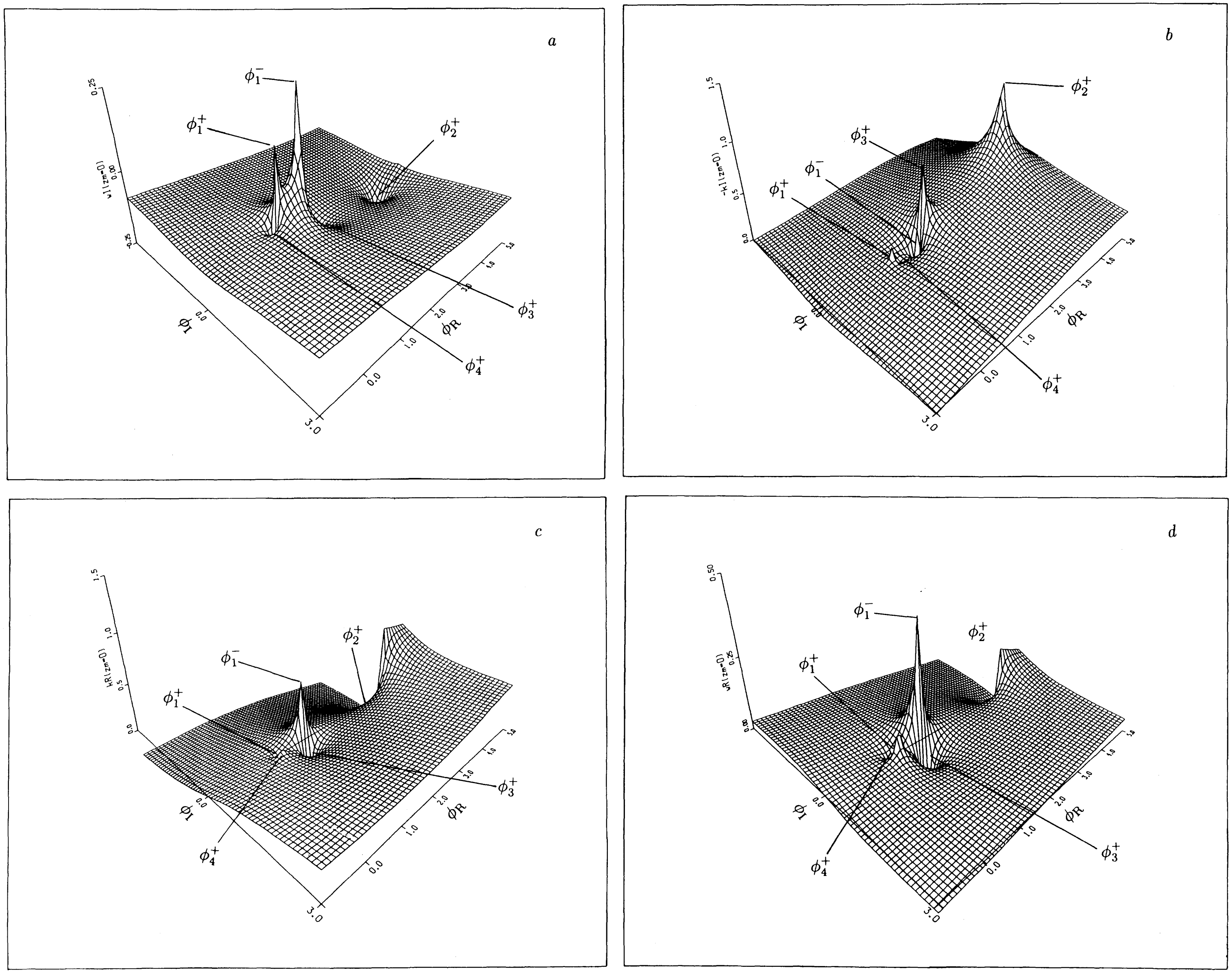

FIG. 3.—The roots extracted from the dispersion equation (eqs. [2]) of a slab jet for symmetric fundamental mode ($zm = 0$). The internal Mach number ($M_{\rm in}$) equals 3; and the density ratio (η) equals 0.1. The roots are plotted on the complex ϕ-plane in the square indicated in Fig. 2(*a*) corresponds to the temporal growth rates (imaginary part of the complex frequency ω). (*b*) Corresponds to the spatial growth rates (negative imaginary part of the complex wavenumber k). (*c*) Corresponds to the real part of the complex frequency ω. (*d*) Corresponds to the real part of the complex wavenumber k.

© American Astronomical Society • Provided by the NASA Astrophysics Data System

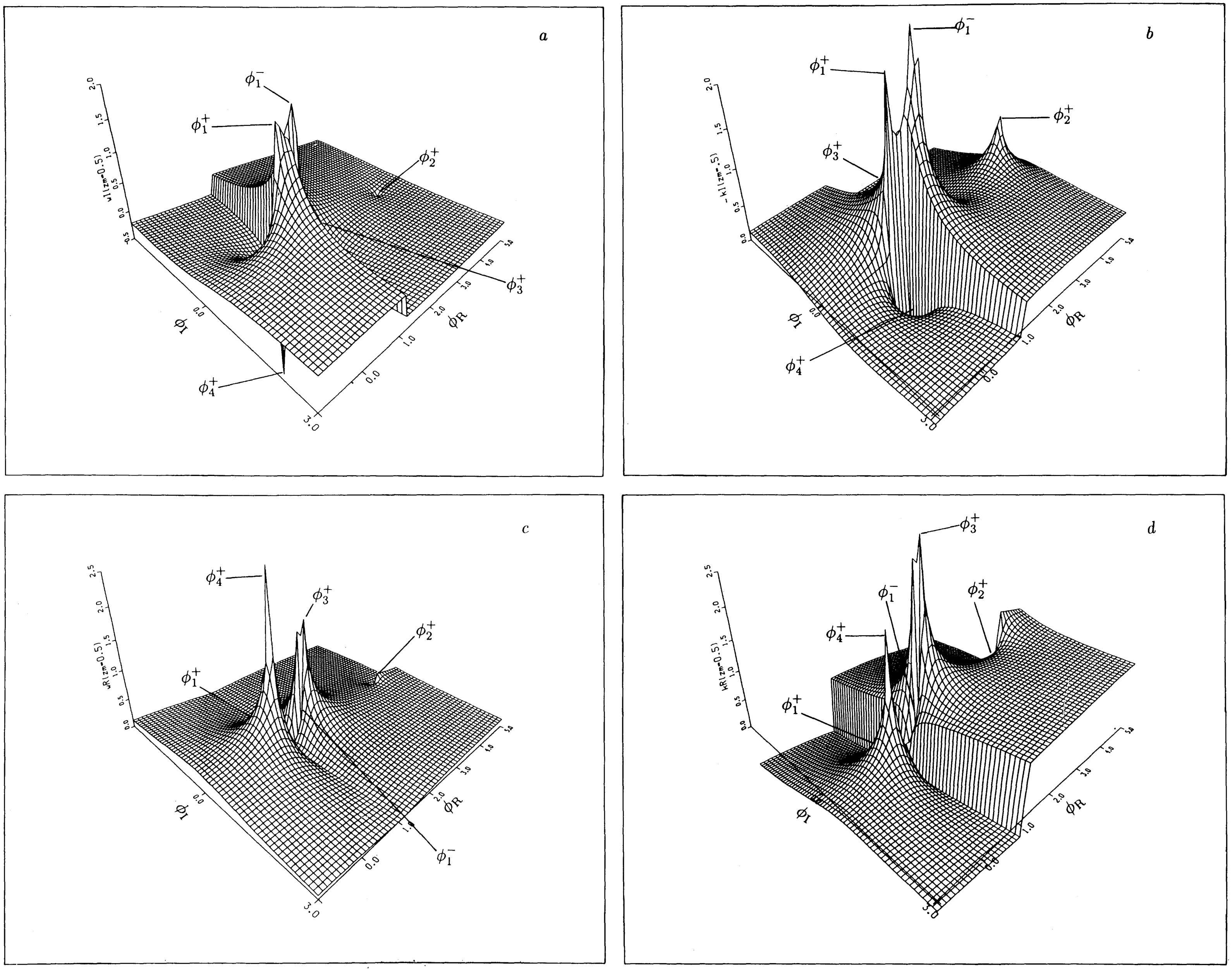

FIG. 4.—The roots extracted from a dispersion equation (eqs. [2]) of a slab jet for antisymmetric fundamental mode (zm = $\frac{1}{2}$). The physical parameters and symbols are the same as in Fig. 3.

© American Astronomical Society • Provided by the NASA Astrophysics Data System

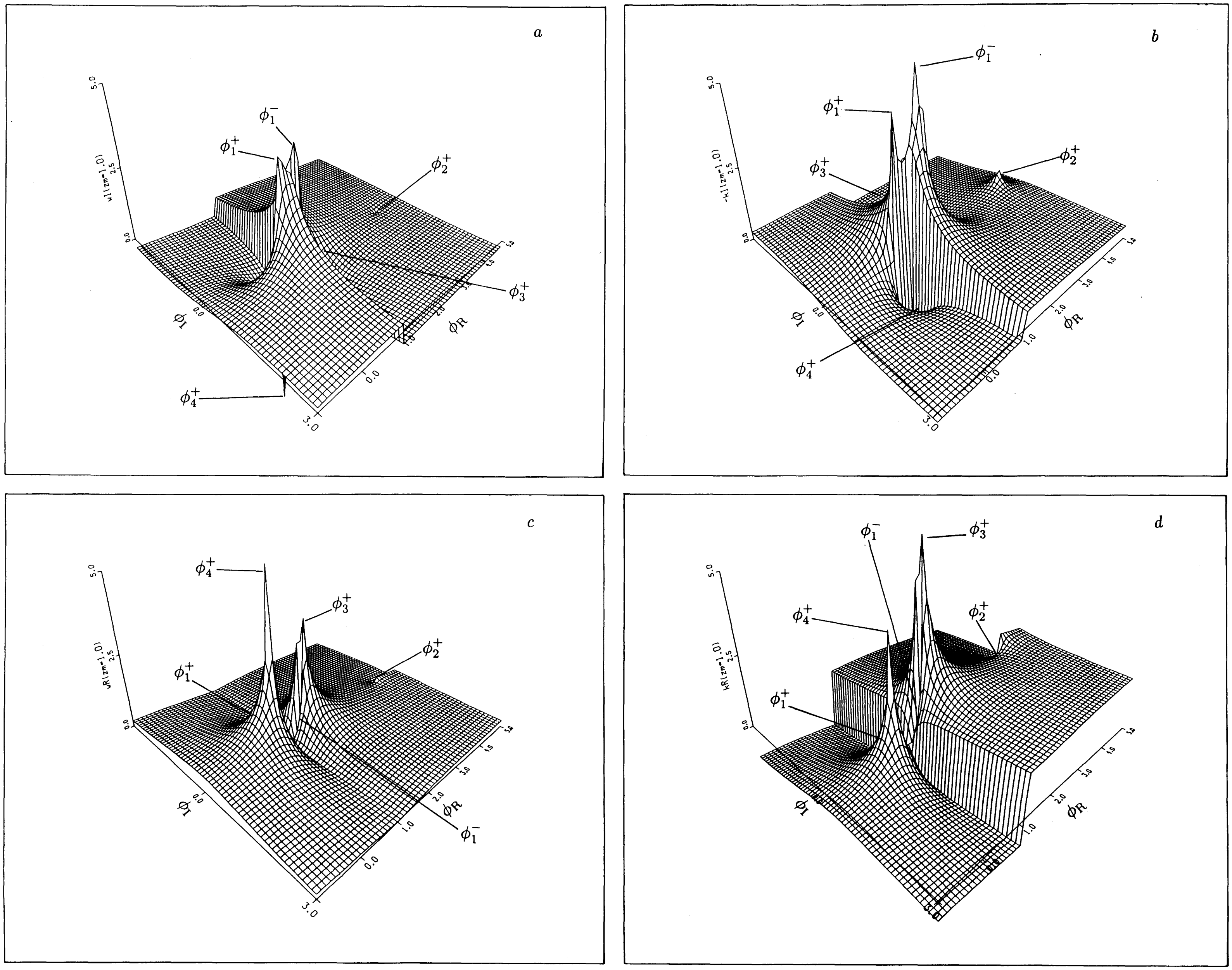

FIG. 5.—The roots solved from the dispersion equations (eqs. [2]) for the reflection modes zm = 1. The physical parameters and symbols are the same as in Fig. 3.

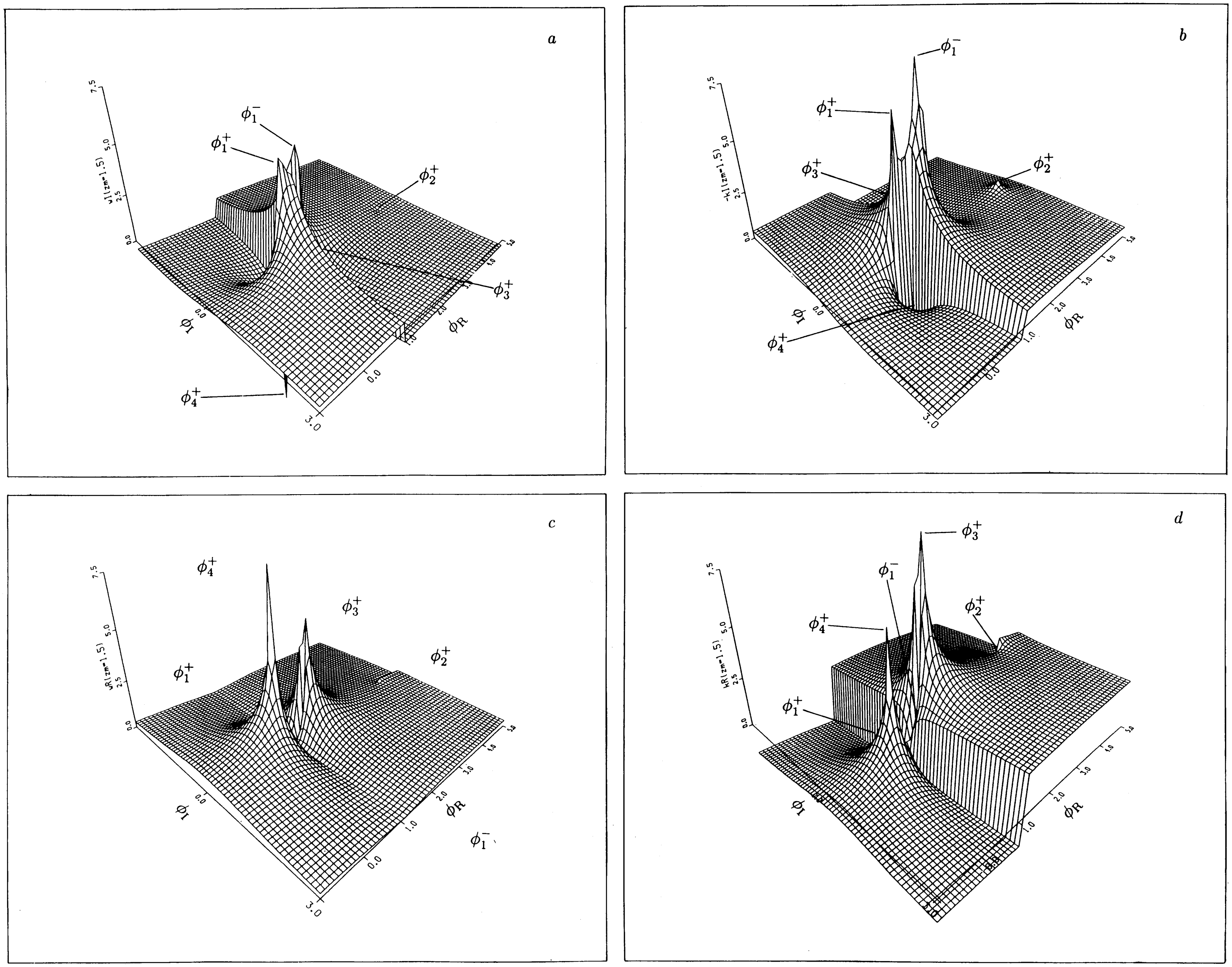

FIG. 6.—The roots solved from the dispersion equations (eqs. [2]) for the reflection modes zm = 3/2. The physical parameters and the symbols are the same as in Fig. 3.

© American Astronomical Society • Provided by the NASA Astrophysics Data System

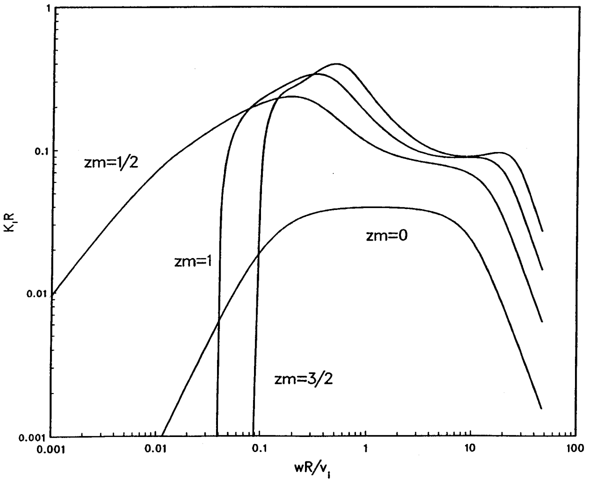

FIG. 7.—The roots with fixed real frequency ω are calculated for the symmetric and antisymmetric fundamental (zm = 0, 1/2), and reflection (zm = 1, 3/2) modes by using a complex roots finder described in text. We plot spatial growth rate vs. frequency based on the roots with fixed real ω perturbation.

which is equivalent to setting the density ratio $\eta = 0$ (i.e., the density of the medium outside jet becomes very large). For this case, the term $\ln(D)$ vanishes in equation (6). The boundary gives rise to only reflection and refraction. Surface waves do not exist. The eight singularities are reduced to two, ϕ_1^+ and ϕ_1^-, associated with acoustic waves propagating against and with the flow, respectively. The phase velocities of the two acoustic waves are $\pm a_{\mathrm{in}}$ (i.e., internal sound speed) in the flow rest frame. Each wave consists of fundamental (zm = 0 or $\frac{1}{2}$) and internal reflection (zm ≥ 1) modes. In this case all the modes are not growing since the interaction with the rigid boundaries only changes the propagation directions of the wave and does not change the wave energy. Second, we consider the case where the density ratio η becomes large (i.e., a jet is unbounded.) In addition to the body waves, we are able to find three other surface waves in this case. One of them is associated with velocity shear, namely, $\phi = 1$ ($v_{\mathrm{ph}} = u_0$). The remaining two are associated with density discontinuities and $v_{\mathrm{ph}} = \pm(\eta)^{1/2} a_{\mathrm{in}}$.

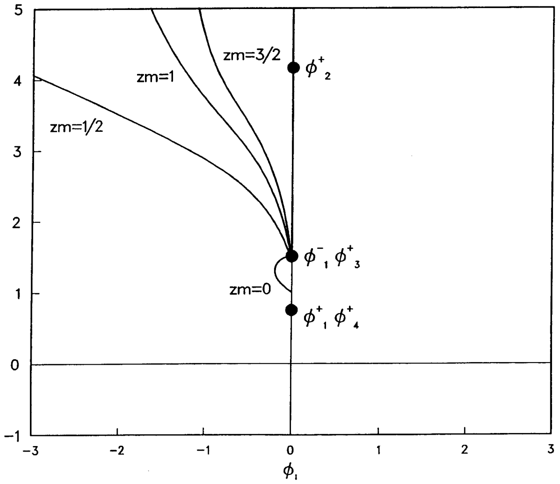

FIG. 8.—We plot the tracks, corresponding to the roots with fixed real ω plotted in Fig. 7, on the ϕ-plane. ω_R increases along the curves labeled zm = 0, 1/2, 1 and 3/2, respectively, toward the points ϕ_1^- and ϕ_3^+.

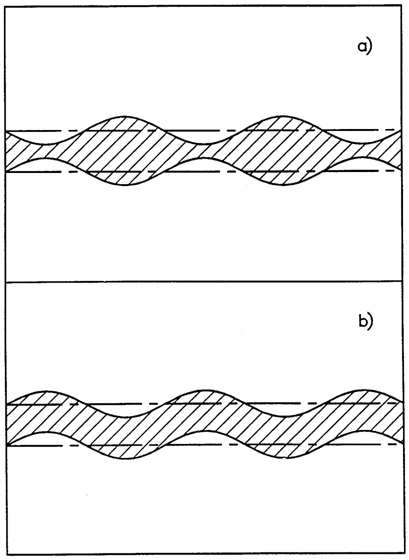

FIG. 9.—(*a*) Surface wave with symmetric geometry propagates along a thermally confined slab jet. (*b*) Surface wave with antisymmetric geometry propagates along a thermally confined jet.

In general, the density ratio η is finite and, therefore, the term $\ln(D)$ in equation (6) is not zero. Thus, in addition to the two body waves existing in the above two cases, there are six surface waves that correspond to the six singularities found in the term $\ln(D)$. In Table 1, we show the properties of the eight waves found in the thermally confined slab jet as the internal jet Mach number M_{in} goes to zero. The first two have been discussed in the previous paragraph. They are acoustic body waves independent of boundary. Here we investigate the nature of the six additional waves. As tabulated in Table 1, we know that the six waves are associated with velocity shear, u_0, and density ratio, η. In other words, the six waves depend on the boundary discontinuities, and therefore, can be identified as surface waves. Thus, K-H instabilities arise at the interface with either velocity shearing and/or density discontinuity between jet and ambient gas (Drazin & Reid 1981). In the supersonic region, each body wave is coupled to a relevant surface wave (see Fig. 1) and may cause an acoustic resonance (in § 2).

5. THE TOTAL GROWTH RATES

In the previous section we discussed the different types of jet boundaries. In a perfectly rigid jet boundary, there are only two acoustic body waves, and the two waves are not growing. Once the jet is thermally confined, the waves become unstable. In § 3, we showed the spatial growth rate ($-\tilde{k}_I$) and the temporal growth rate ($\tilde{\omega}_I$) in the ϕ-plane. In the complex ($\tilde{k}, \tilde{\omega}$)

TABLE 1

PROPERTIES OF THE WAVES IN A THERMALLY CONFINED SLAB JET ($M_{\mathrm{in}} \rightarrow 0$)

ϕ	v_{ph}	Wave Type
$\phi_1^\pm = M_{\mathrm{in}}/(M_{\mathrm{in}} \pm 1)$	$v_j \pm a_{\mathrm{in}}$	acoustic body
$\phi_2^\pm = 1 \pm \eta^{-1/2}$	$\eta^{1/2}(\eta^{1/2} \pm 1)^{-1} v_j$	surface
$\phi_3^\pm = 1 \pm i\eta^{-1/2}$	$(1 \mp i\eta^{-1/2})(1 + \eta^{-1/2})^{-1} v_j$	surface
$\phi_4^\pm = \pm(1 + \eta)^{-1/2} M_{\mathrm{in}}$	$\pm(1 + \eta)^{1/2} a_{\mathrm{in}}$	surface

domain, the spatial and temporal growth rates are no longer independent. Thus, the total growth rate is a function of $\tilde{k}$ and $\tilde{\omega}$.

Let us discuss the total growth rate based on a single mode. In the complex $(\tilde{k}, \tilde{\omega})$ domain, a single normal mode can be written as

$$\begin{aligned} f &= A \exp\{i(kz - wt)\} \\ &= A \exp\{i(\tilde{k}_R \tilde{z} - \tilde{\omega}_R \tilde{t})\} \exp(-\tilde{k}_I \tilde{z} + \tilde{\omega}_I \tilde{t}) ; \end{aligned} \tag{15}$$

where $\tilde{z} = z/R$ and $\tilde{t} = tu_0/R$ are dimensionless spatial and temporal coordinates. The first term on the right side of equation (15) is simple oscillation. The second term represents the instability behavior of the normal mode. The total spatial growth can be investigated by using the dimensionless phase velocity $\tilde{v}_{\rm ph} = \tilde{\omega}_R/\tilde{k}_R$, and holding the phase constant along a characteristic line with a slope of $\tilde{v}_{\rm ph}$ (i.e., setting the $\tilde{z}/\tilde{t} = \tilde{v}_{\rm ph}$) to see whether it is growing or not. To measure the total spatial growth rate of the mode, we rewrite the second term on the right side of equation (15) as $\exp[(-\tilde{k}_I + \tilde{\omega}_I \tilde{k}_R/\tilde{\omega}_R)\tilde{z}]$. Therefore, the total spatial growth rate is given by

$$R_s = -\tilde{k}_I + \tilde{\omega}_I \tilde{k}_R/\tilde{\omega}_R ; \tag{16}$$

The first term is just the spatial growth without the contribution from the temporal growth. In the complex $(\tilde{k}, \tilde{\omega})$ domain, the temporal growth contributes to the total spatial growth because in the observer's frame the growing energy indicated by the temporal growth $\tilde{\omega}_I$ is carried downstream by the waves, and this leads to the second term on right side of equation (16). Thus, a total dimensionless e-folding length is defined by $\tilde{l}_e = (-\tilde{k}_I + \tilde{\omega}\tilde{k}_R/\tilde{\omega}_R)^{-1}$. Similarly, a total dimensionless temporal growth rate is given as

$$R_t = -\tilde{k}_I \tilde{\omega}_R/\tilde{k}_R + \tilde{\omega}_I ; \tag{17}$$

and the total e-folding time is $\tilde{\tau}_e = (-\tilde{k}_I \tilde{\omega}_R/\tilde{k}_R + \tilde{\omega}_I)^{-1}$. The stability of the mode is determined by the sign of the growth rate. From equations (16) and (17), we know that the signs of spatial and temporal growth are identical and are determined by $(-\tilde{k}_I \tilde{\omega}_R + \tilde{k}_R \tilde{\omega}_I)$. If $(-\tilde{k}_I \tilde{\omega}_R + \tilde{k}_R \tilde{\omega}_I) > 0$, the mode is exponentially growing. If it equals zero, the mode does not grow. If it is less than zero, the mode exponentially decays.

In addition to the sign of the growth rate, the magnitude of the total growth rate $(R_{\rm tot})$ must be defined. Figure 10 shows the growth behavior of a single mode at a fixed phase. Clearly, the magnitude of the total growth is determined by the combination of the e-folding length $(\tilde{l}_e)$ and e-folding time $(\tilde{\tau}_e)$

$$|R_{\rm tot}| = \frac{1}{\sqrt{\tilde{l}_e^2 + \tilde{\tau}_e^2}} .$$

In general, the total growth rate can be expressed in the form:

$$R_{\rm tot} = \frac{-\tilde{k}_I \tilde{\omega}_R + \tilde{k}_R \tilde{\omega}_I}{\sqrt{\tilde{\omega}_R^2 + \tilde{k}_R^2}} . \tag{18a}$$

And the second term on the right side of equation (15) can be rewritten as a form of $\exp[R_{\rm tot}(\tilde{z}^2 + \tilde{t}^2)^{1/2}]$. Using the relations $\tilde{k}_R = \tilde{\omega}_R \phi_R - \tilde{\omega}_I \phi_I$ and $\tilde{k}_I = \tilde{\omega}_R \phi_I + \tilde{\omega}_I \phi_R$, we can express the total growth rate as

$$R_{\rm tot} = \frac{-\phi_I(\tilde{\omega}_R^2 + \tilde{\omega}_I^2)}{\sqrt{\tilde{\omega}_R^2 + \tilde{k}_R^2}} , \tag{18b}$$

where ϕ_I is the imaginary part of ϕ. Equation (18b) shows that the unstable modes with total growth greater than zero are located on the $\phi_I < 0$ portion of the ϕ-plane. Along the real axis of the ϕ-plane, the mode does not grow. On the $\phi_I > 0$ portion of the plane, the modes exponentially decay.

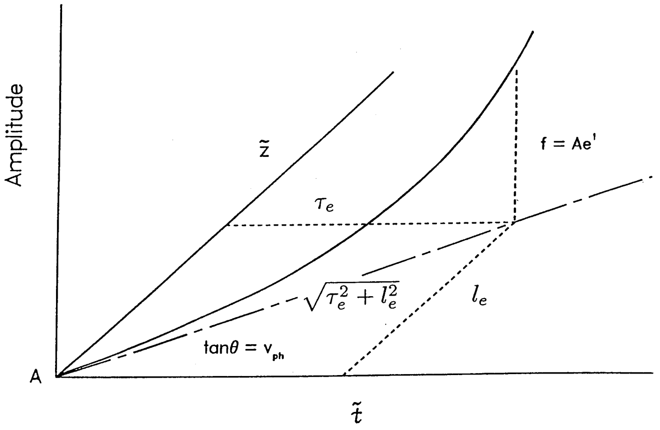

FIG. 10.—A single mode grows exponentially in amplitude along the characteristic line with a slope $v_{\rm ph}$ in a $(\tilde{z}, \tilde{t})$ plane.

In Figure 11, we present calculations of the total growth rate in the ϕ-plane for zm = 0, 1/2, 1, and 3/2. Here we show those modes with $\tilde{k}_R > 0$. The zm = 0 mode has different structure from nonzero zm modes. It is interesting that the growing symmetric fundamental modes (zm = 0) are located only around the singularities of the acoustic wave propagating against the flow. Note the other singularities in zm = 0 mode are associated with the evanescent modes which can usually be neglected.

The structures in the total growth rate curves are similar among the nonzero zm modes except that the amplitude increases as zm increases. The fast-growing modes locate around the acoustic singularities, propagating both against and along the flow. It is clear that the acoustic body waves in the thermally confined jet must grow. The surface waves coupling to the acoustic body waves also grow. These waves increase in amplitude and eventually disrupt the jet. We note that between the two singularities there is a gap where no growing modes are found. This suggests that the two body waves can be distinguished in the space and time domain. The acoustic wave propagating against the flow travels slowly with an average velocity $u_0 - a_{\rm in}$. The acoustic wave propagating along the flow travels quickly with an average velocity $u_0 + a_{\rm in}$.

In general, a perturbation imposed upon an initially steady jet flow excites all of the modes. The transient modes located on the $\phi_I > 0$ portion of the ϕ-plane decay exponentially after the initial excitation. The growing modes are associated with the acoustic body waves as well as the relevant surface waves. It has been pointed out by Payne & Cohn (1985) that a confined jet acts as an acoustic wave guide. The sound waves impinging on the interface between the jet and the surrounding medium interfere with reflected waves. The interactions lead to large changes in wave energy which comes from the difference in bulk kinetic energy across the jet boundary (Gill 1965). Gain or loss of the energy carried by the sound waves in the interactions with the interface is determined by the sign of the wave velocities in the jet's frame. The waves propagating against the jet will gain energy through the cascade scattering, and the amplitudes of the wave modes will grow; while the waves pro-

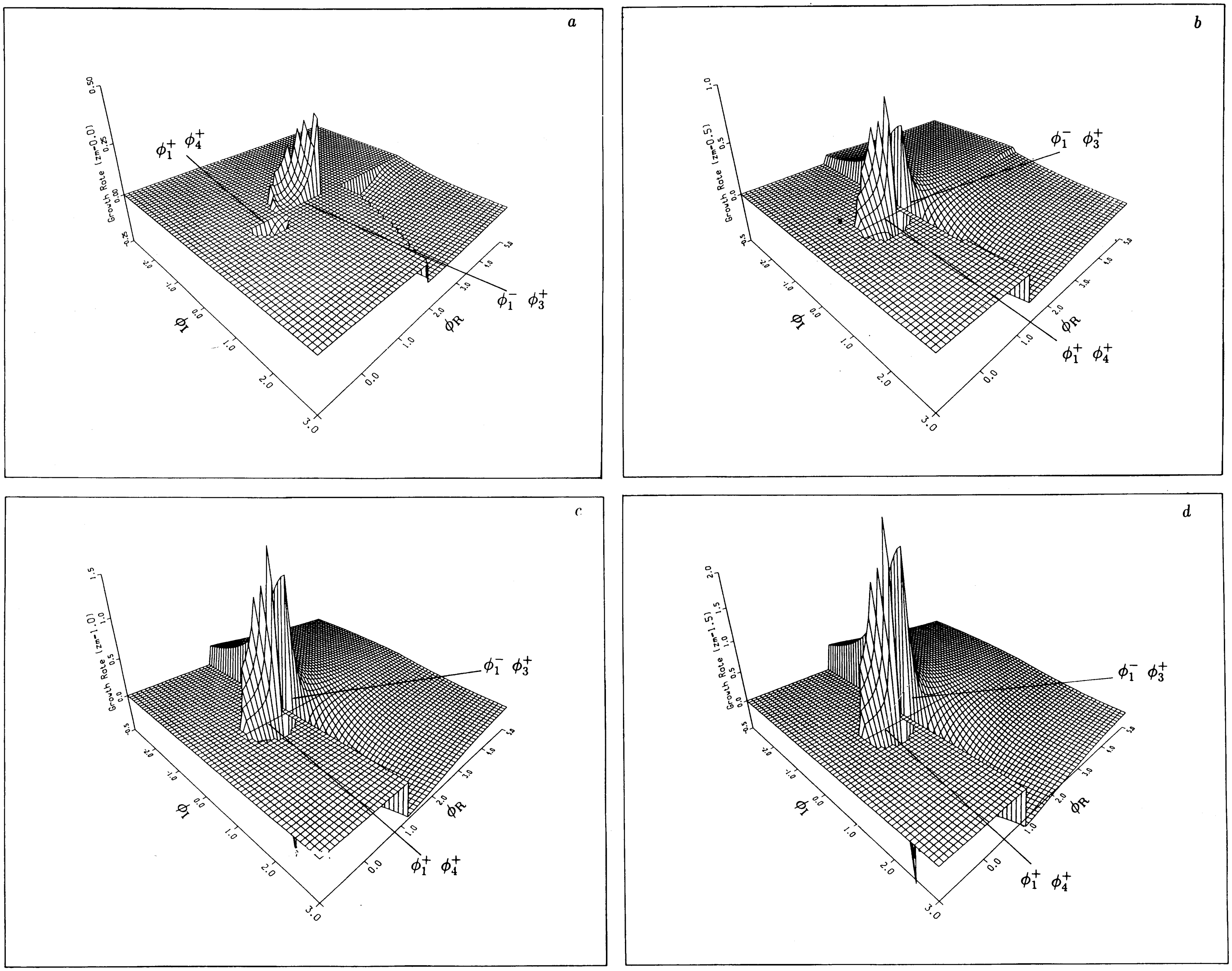

FIG. 11.—Total growth rates are plotted for zm = 0, 1/2, 1, and 3/2 modes in the ϕ-plane

© American Astronomical Society • Provided by the NASA Astrophysics Data System

pagating with the jet will lose internal energy to the ambient gas through the cascade scattering and the negative amplitudes of the wave modes will also grow. In other words, the internal acoustic body wave propagating against the jet is a condensed wave and the internal acoustic body wave propagating with the jet is a rarefied wave. We have verified this inference with numerical simulations in Paper II.

Thus, the effects of reflection are crucial to the growing internal body waves and surface waves. To each reflection mode, there is a cutoff wavenumber $\tilde{k}_c = \mathrm{zm}\pi/(M_{\mathrm{in}}^2 - 1)^{1/2}$ (Hardee & Norman 1988) which corresponds to a cutoff wavelength. At the wavelengths exceeding the relevant cutoff, the reflection modes become evanescent. In the other words, the effects of reflection appear only at the shorter wavelengths. In addition, at a short wavelength, say less than the velocity shear scale length, the energy spectrum of a general perturbation is substantially suppressed. Thus, the significant reflection modes are effectively the first few orders (zm = 1 and 3/2). Therefore, the first-order reflection modes in both symmetric and antisymmetric cases are suggested to govern the general growth rate of the system.

In our numerical simulations, we have shown that the growing wave modes propagate in phase velocities centered at $u_0 - a_{\mathrm{in}}$ or $u_0 + a_{\mathrm{in}}$ (see Paper II, § 4.2). This agrees well with the linear analysis, where both symmetric and antisymmetric reflection modes have been predicted. We note that quantitative application of the growth of the waves predicted in the linear analysis to astrophysical observations has been achieved via a combination of numerical simulations and other nonlinear theory (i.e., characteristic theory of fluid dynamics; see Paper II). It should be noted that individual modes whose total growth rates are plotted in Figure 11 cannot be directly seen in either numerical simulations or astrophysical observations because of superposition of the many wave modes and other effects. However, the numerical simulations indicate that the first few orders of modes effectively dominate the system, and the average of the growth rates in Figure 11 agrees quite well with the numerical simulations.

It is clear now that internal sound waves grow in a thermally confined jet. The two distinguishable growing waves propagate with average velocities $u_0 - a_{\mathrm{in}}$ and $u_0 + a_{\mathrm{in}}$ in the observer rest frame. Investigating the two acoustic waves in numerical simulations is crucial in understanding the disruption of jets. The linear behavior of the distinguishable acoustic body and relevant surface waves will be examined via numerical simulations in Paper II.

6. DISCUSSION AND SUMMARY

6.1. *Discussion*

We have solved the dispersion relation of a thermally confined slab jet in the complex (k, ω) domain. Our analysis has demonstrated an association of the physical waves with unstable modes in the system. This work is also a useful complement to the previous work in the comprehension of the wave phenomena in jets. An understanding of the wave characteristics is crucial for comparing linear theory with simulations and observations. We note that the linear study of a thermally confined slab jet provides the fundamental physics to understand the features appearing in the numerical simulations and astronomical observations, although it is not a perfect model to fit a specific observed jet.

The instability and disruption of the jets have now been seen in both radio observations and numerical simulations. In the present work, we have established a number of important points regarding the instability of body and surface waves in the jet. The growing body waves should be dominant in the linear stage of evolution of jet instabilities. The two waves are distinguishable by their average velocity $u_0 - a_{\mathrm{in}}$ and $u_0 + a_{\mathrm{in}}$. In fact, the body and the relevant surface waves propagating against the flow have been observed as a fast growing wave pattern in jet simulations (Norman et al. 1984). The speeds given by Norman et al. are systematically smaller than $u_0 - a_{\mathrm{in}}$ because their measurements were made in a partially nonlinear stage. The waves in that stage become nonlinear and the jet starts to disrupt. The growth of the waves slow down their propagation speeds. The body and the relevant surface waves propagating along the flow have been ignored because they are rarefied in density (or internal energy) and propagate faster (See Paper II). In other words, the body waves propagating along the jet are relatively unimportant in jet disruptions.

Finally, we discussed the implication of this work to observations of astrophysical jets. At the VLA scale, a number of radio jets have been found in clusters of galaxies which wiggle, flare, and then disrupt forming diffuse lobes or tails (Perley, Wills, & Scott 1979; O'Donoghue, Owen, & Eilek 1990). These data may suggest that such jets are subject to K-H instabilities. The waves initially perturbed in the jet exponentially grow and propagate to the outer region until the "pipeline" is disrupted. Recently, high-resolution and high-dynamic range VLA observation of M87 show that the jet in this source is limb-brightened over much of its length and bright filaments appear to be located on the surface (Owen, Hardee, & Conwell 1989). Our analysis of the stability of thermally confined jets reveals the existence of unstable surface waves along the jet boundary. The wave interaction along the boundary of a jet may provide the environment for particle acceleration along the surface. This might explain why the bright filaments in a jet like M87 are embedded in the surface of jet.

6.2. *Summary*

In an effort to understand the instabilities and disruptions of astrophysical jets propagating in the galaxy ISM and cluster ICM, we have investigated Kelvin-Helmholtz instabilities for a thermally confined slab jet in a more generalized fashion than in previous studies. We have solved the dispersion equations in a complex (k, ω) domain. Several interesting results are summarized here.

First, we have found a number of singularities in the system. Two of them are associated with two internal sound waves propagating along two distinguishable characteristic lines with slopes $u_0 - a_{\mathrm{in}}$ and $u_0 + a_{\mathrm{in}}$ in an observer rest frame. The confined jet is just like an acoustic wave guide and the internal sound waves impinge on the boundary from one side of jet to the other. Gain or loss the energy carried by the internal sound waves during the scattering with the interface is determined by the sign of the wave velocities in the jet rest frame. The sound wave propagating with the jet is a growing rarefied body wave and the sound wave propagating against the jet is a condensed body wave. In the linear stage, the internal jet flow in the system is characterized by the two acoustic body waves with superposition of certain reflection patterns. In addition to internal body waves, we recognize a number of surface waves in the system. Two of them are coupled to the relevant body waves. The surface waves also grow in amplitude, developing abundant dynamical vortices along the surface.

1992ApJ...387...69Z

Second, there is a critical condition, $M_{\rm in}^2 > \eta + 1 + \eta^{1/3} M_{\rm in}^{2/3}$, under which the jet becomes supersonic and the eight singularities found in the system are real. Once the jet becomes transonic, $M_{\rm in}^2 < \eta + 1 + \eta^{1/3} M_{\rm in}^{2/3}$, two of the singularities form a complex conjugate pair and the structure of the roots becomes more complicated. With a broad spectrum derived in this paper, we now have a better understanding of the distribution of singularities in the system.

Finally, the analysis in this paper provides a self-consistent model to interpret the wealth of phenomena observed in astrophysical jets. The abundant growing surface waves found here possibly correspond to limb-brightened features and surface filaments discovered in astrophysical jets. We will show that disruptions of supersonic jets can be caused by growing internal acoustic body waves, as well as the relevant surface waves, propagating against flow in our Paper II. The quasi-periodic wiggles and abrupt flares observed in jets are natural consequences of the growth of surface and body waves.

We thank Martin Sulkanen, David Clarke, Dean Sumi, and Q.-F. Yin for their useful discussions and comments. J.-H. Z. wishes to acknowledge the University of New Mexico for support during the course of this thesis research. This research was supported by NSF grants AST-8611511 and AST-9012353 to J. O. B. and M. L. N. In addition, P. E. H. acknowledges support from the National Science Foundation through EPSCoR grant RII-8610699 and NSF grant AST-8919180 to the University of Alabama.

REFERENCES

Blandford, R. D., & Pringle, J. E. 1976, MNRAS, 176, 443
Blandford, R. D., & Rees, M. J. 1974, MNRAS, 169, 395
Burns, J. O., Norman, M. L., & Clarke, D. A. 1986, in Proc. NRAO Workshop 16, Radio Continuum Processes in Clusters of Galaxies, ed. C. P. O'Dea & J. M. Uson (Green Bank: NRAO), 175
Cohn, H. 1983, ApJ, 269, 500
Drazin, P. G., & Reid, W. H. 1981, in Hydrodynamic Stability (Cambridge Univ. Press)
Ferrari, A., Trussoni, E., & Zaninetti, L. 1978, A&A, 64, 43
———. 1981, MNRAS, 196, 1054
———. 1982, MNRAS, 198, 1065
Gaster, M. 1965, J. Fluid Mech., 22, 433
Gill, A. E. 1965, Phys. Fluids, 8, 1428
Hardee, P. E. 1979, ApJ, 254, 47
———. 1982, ApJ, 257, 509
———. 1983, ApJ, 269, 94
———. 1984, ApJ, 287, 523
———. 1986, ApJ, 303, 111
Hardee, P. E. 1987, ApJ, 313, 607
Hardee, P. E., & Norman, M. L. 1988, ApJ, 334, 70
Miles, J. W. 1957, J. Acoust. Soc. Am. 29, 226
Miles, J. W., & Fejer, J. A. 1963, J. Fluid Mech., 15, 335
Norman, M. L., Burns, J. O., & Sulkanen, M. 1988, Nature, 335, 146
Norman, M. L., & Hardee, P. E. 1988, ApJ, 334, 80
Norman, M. L., Winkler, K. H., & Smarr, L. L. 1984, in Proc. NRAO Workshiop 9, Physics of Energy Transport in Extragalactic Radio Sources, ed. A. H. Bridle & J. A. Eilek (Greenbank: NRAO), 150
O'Donoghue, A. A., Owen, F. N., & Eilek, J. A. 1990, ApJS, 72, 75
Owen, F. N., Hardee, P. E., & Conwell, T. J. 1989, ApJ, 340, 698
Payne, D. G., & Cohn, H. 1985, ApJ, 291, 655
Perley, R. A., Wills, A. G., & Scott, J. S. 1979, Nature, 281, 437
Ray, T. P. 1981, MNRAS, 196, 195
Scheuer, P. A. G. 1974, MNRAS, 166, 513
Zhao, J.-H., Burns, J. O., Norman, M. L., & Sulkanen, M. 1992, ApJ, 387, 83 (Paper II)

© American Astronomical Society • Provided by the NASA Astrophysics Data System